Journal of Materials Chemistry C

ROYAL SOCIETY OF CHEMISTRY

PAPER

View Article Online
View Journal | View Issue

Cite this: J. Mater. Chem. C, 2025, 13, 18905

Stress-coupled spin state switching in a spin crossover composite modulates current in an organic semiconductor

Yuteng Zhang,[ab] Aurelian Rotaru,[c] Thomas Ranquet,[b] Xinyu Yang,[a] Yue Zan,[a] Benjamin Reig,[b] Isabelle Séguy,[b] Lionel Salmon,[a] Gábor Molnár *[a] and Azzedine Bousseksou*[a]

The combination of spin-crossover (SCO) complexes with electrically conducting materials offers a promising route for developing stimuli-responsive electronics, yet the mechanism of charge transport modulation remains unexplored. Here, we investigate a bilayer heterostructure comprising silica-coated SCO nanoparticles $[Fe(Htrz)_2(trz)](BF_4)@SiO_2$ within a polyvinylpyrrolidone (PVP) matrix and organic semiconductors (OSCs), where mechanical stress generated by spin-state switching within the PVP:SCO layer modulates the conductance within the OSC layer. Through *in situ* piezo-resistivity characterization, we reveal a reversible conductance modulation in the OSC layer under hydrostatic pressure, providing a quantitative evaluation of pressure-induced stress sensitivity with the OSC layer. Crucially, the intrinsic properties of the SCO nanoparticles dictate key characteristics of the switching device such as the spin transition temperature and hysteresis width, enabling tunable and non-volatile memory behavior. Demonstrating robust switching over multiple thermal cycles—rooted in the intrinsic thermal stability of the SCO and validated by X-ray diffraction/optical spectroscopy analysis at elevated temperatures—this work lays the groundwork for a new class of stress-coupled spin-electronic systems, offering a potential route for the development of piezo-resistive sensors and adaptive memory devices.

Received 2nd June 2025,
Accepted 30th July 2025

DOI: 10.1039/d5tc02153g

rsc.li/materials-c

Introduction

Molecular switches have emerged as a class of promising materials for next-generation electronics, offering unique functionalities for information storage, logic operations, and neuromorphic computing applications.[1–4] Among these, spin-crossover (SCO) complexes of $3d^4$–$3d^7$ transition metal ions have garnered significant attention due to their ability to reversibly switch between low-spin (LS) and high-spin (HS) states under external stimuli such as temperature, pressure, light, or molecular binding.[5–7] The spin-state transition is accompanied by dramatic changes in magnetic susceptibility, optical absorption, electronic polarizability, and mechanical behavior, enabling a broad range of multifunctional device possibilities.[3,8–13]

In addition to the direct use of SCO properties, the integration of SCO materials into hybrid architectures with electroactive compounds—such as graphene, metallic nanoparticles, molecular conductors, piezoelectric, or ferroelectric materials—has opened new avenues for responsive and reconfigurable electronics.[11,14–25] In these systems, the SCO component can serve as a stimulus-sensitive element, while the electronic counterpart transduces the spin-state switching effect. Among possible configurations, organic semiconductors (OSCs) are particularly compelling due to their mechanical flexibility, low-cost processing, and wide use in printed and stretchable electronics.

In a recent study, we demonstrated that the spin-state switching of $[Fe(Htrz)_2(trz)](BF_4)@SiO_2$ nanoparticles embedded in a polyvinylpyrrolidone (PVP) matrix could modulate the charge carrier mobility in a poly(3-hexylthiophene) (P3HT)-based organic field-effect transistor (OFET).[23] This effect was attributed to mechanical stress induced in the OSC layer by the volume expansion of the SCO particles during the spin transition, as supported by finite element analysis. However, direct experimental validation of this stress-coupled transport mechanism was challenging due to the fragility of OFET devices.

In the present work, we address this limitation by developing a robust two-terminal device platform based on interdigitated electrodes (IDEs), enabling *in situ* electrical and piezo-resistive

[a] LCC, CNRS and Université de Toulouse, UPS, INP, F-31077 Toulouse, France. E-mail: gabor.molnar@lcc-toulouse.fr, azzedine.bousseksou@lcc-toulouse.fr
[b] LAAS-CNRS, Université de Toulouse, CNRS, Toulouse, France
[c] Faculty of Electrical Engineering and Computer Science and MANSiD Research Center, Stefan cel Mare University, 13, Strada Universitatii, Suceava 720229, Romania

measurements. To enhance signal levels, we employ ethanesulfonic acid (ESA)-doped P3HT, which significantly improves the conductivity of the OSC film. The PVP:SCO layer, composed of $[Fe(Htrz)_2(trz)](BF_4)$@SiO_2 nanoparticles dispersed in a PVP matrix, is deposited at the top of the OSC layer to form a bilayer architecture. Under thermal cycling, we observe a clear and reversible current modulation (25 ± 3%) in the OSC channel that correlates with the SCO transition. Transport measurements under an applied hydrostatic pressure of 160 MPa confirm a 97 ± 3% change in conductance for the acid-doped P3HT layer, supporting the proposed stress-coupling mechanism.

This approach offers a compelling alternative to conventional current modulation strategies in organic semiconductors (OSCs), which typically rely on gate voltages, chemical doping, magnetic fields, or piezoelectric effects. Each of these methods presents inherent trade-offs, for example, field-effect devices often require high gate voltages and are prone to leakage currents;[26] chemical doping may be irreversible or unstable;[27] spintronic approaches, such as giant magnetoresistance, demand highly precise multilayer fabrication and interface control;[28] and piezoelectric-based modulation relies on intrinsic polarization in ferroelectric or piezoelectric materials, which may involve domain alignment.[29] In contrast, the spin-state switching in SCO materials provides an externally driven, bistable, and non-volatile mechanism for modulating conductivity—without requiring intrinsic dipoles, polar crystal structures, *etc.* Our results establish a new paradigm in hybrid organic electronics, where molecular spin transition serves as programmable mechanical stimuli to modulate charge transport in OSC layers.

Results and discussion

The structure of SCO compound $[Fe(Htrz)_2(trz)](BF_4)$ is shown in Fig. 1a and silica shelled $[Fe(Htrz)_2(trz)](BF_4)$ nanoparticles were synthesized as described in ref. 30. This benchmark SCO compound was chosen for its robust and abrupt spin transition with hysteresis, which occurs above room temperature.[30] The size of the $[Fe(Htrz)_2(trz)](BF_4)$@SiO_2 nanoparticles was modulated by controlling synthesis parameters (temperatures, *etc.*), yielding nanoparticles with distinct sizes, *e.g.* SCO 1 (average length ≈ 50 nm and width ≈ 30 nm) and SCO 2

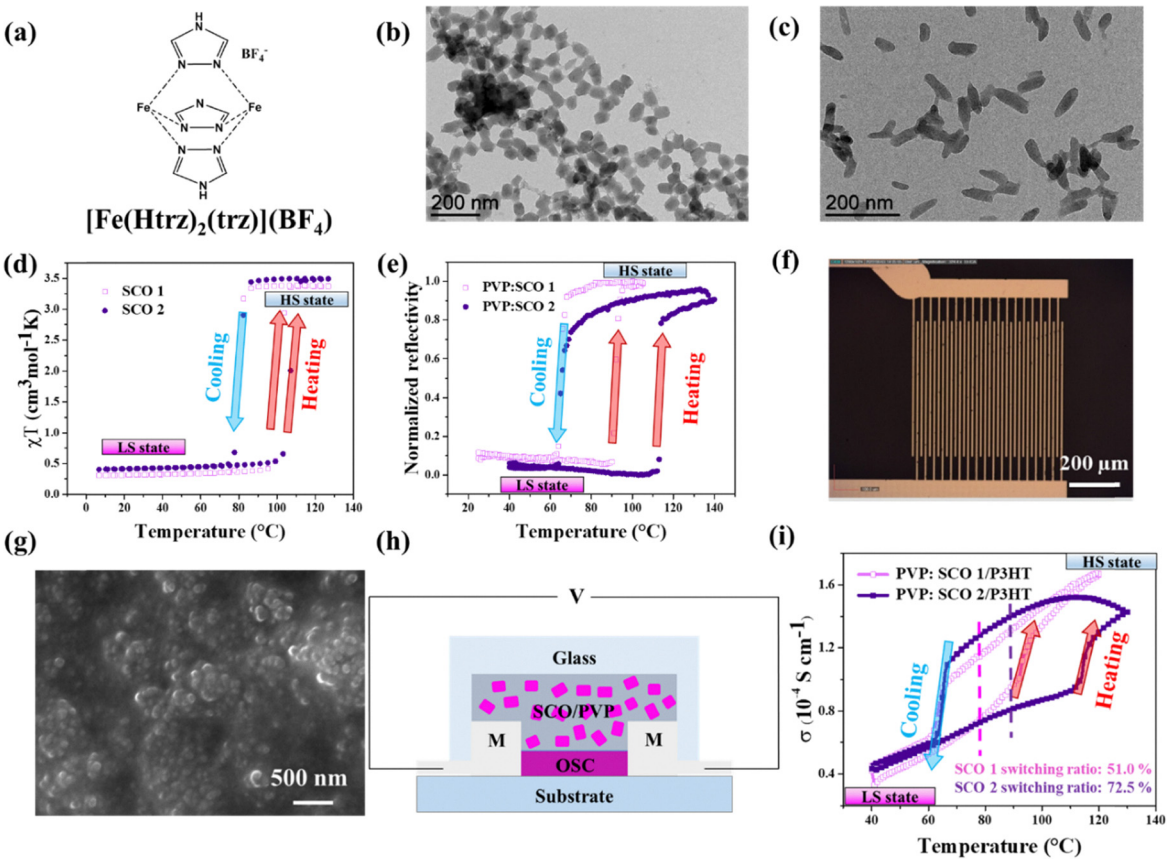

Fig. 1 (a) The structure of the SCO complex $[Fe(Htrz)_2(trz)](BF_4)$. TEM images of the $[Fe(Htrz)_2(trz)](BF_4)$@SiO_2 nanoparticles obtained by controlling the synthesis parameters show (b) smaller sized (SCO 1) and (c) larger sized (SCO 2) nanoparticles. (d) Variable temperature magnetic data for SCO 1 and SCO 2. (e) Temperature-dependent optical reflectivity charaterization of PVP:SCO composite samples. (f) Optical photograph of an IDE substrate. (g) A representative SEM image of the PVP:SCO 1 composite layer, deposited on the top of OSCs using spincoating. (h) A schematic cross-section of a PVP:SCO/OSC IDE device. M represents metal electrodes. (i) Representative temperature-dependent conductance characterization of the PVP:SCO/pristine P3HT devices (dT/dt = ±5 °C min^{-1}). The dashed line indicates the midpoint temperature of the hysteresis loops, shown as a visual guide.

(average length ≈ 70 nm and width ≈ 25 nm). Transmission electron microscopy (TEM) images of these nanoparticles are shown in Fig. 1b and 1c, respectively. High-resolution TEM (HRTEM) confirmed the presence of a thin SiO_2 shell (*ca.* 1–3 nm) surrounding the SCO nanoparticles (see Fig. S1 in the SI). Temperature-dependent magnetic susceptibility measurements (Fig. 1d) revealed that the SCO 1 powder exhibited spin transition temperatures at 80 °C ($T_{1/2\downarrow}$ when cooling) and 99 °C ($T_{1/2\uparrow}$ when heating). Regarding the SCO 2 powder sample, it showed a slightly wider temperature hysteresis compared to the SCO 1 powder sample, with spin transition temperatures at 80 °C ($T_{1/2\downarrow}$ when cooling) and 107 °C ($T_{1/2\uparrow}$ when heating). These different SCO behaviors were further corroborated by temperature-dependent reflectivity measurements (Fig. 1e) on the PVP:SCO composites. The PVP:SCO 1 composite displayed a $T_{1/2\downarrow}$ at 62 °C and $T_{1/2\uparrow}$ at 92 °C (30 °C hysteresis), while the PVP:SCO 2 composite showed a $T_{1/2\downarrow}$ at 62 °C and $T_{1/2\uparrow}$ at 112 °C (50 °C hysteresis). A slight shift in the SCO behavior between the powder and composite samples was observed, consistent with previous reports which revealed similar differences in other SCO systems.[16,31,32] A first series of PVP:SCO/OSC IDE devices were fabricated using pristine P3HT as the conduction layer. An example of one IDE device is shown in Fig. 1f (see also Fig. S2 in the SI). The SCO composite/P3HT films were deposited on the device successively. Scanning electron microscopy (SEM) characterization of the surface morphology (Fig. 1g) confirmed that the PVP:SCO 1 composite nanoparticles formed a continuous top layer, ensuring full surface coverage.

The schematic cross-section of the PVP:SCO/OSC interdigitated electrode (IDE) device is illustrated in Fig. 1h. The device consists of an organic semiconductor (OSC) layer deposited between two platinum electrodes, with a top layer of the PVP:SCO composite. The PVP:SCO layer does not contribute to the measured current, as both the SCO particles and PVP are inherently insulating materials. A voltage bias was applied to the electrodes, while temperature was varied to control the spin states of the SCO material. This setup allowed us to investigate the effect of the SCO phenomenon on charge transport within the conducting layer (OSC layer) by monitoring the temperature-dependent current characteristics. As shown in Fig. 1i, a complete heating–cooling cycle was performed on both SCO 1 and SCO 2 composites-based IDE devices. The results revealed a pronounced increase in conductivity at elevated temperatures, followed by an abrupt drop at lower temperatures ($T_{1/2\downarrow}$ at 63 °C and $T_{1/2\uparrow}$ at 93 °C for the PVP:SCO 1/P3HT-IDE device and $T_{1/2\downarrow}$ at 65 °C and $T_{1/2\uparrow}$ at 115 °C for the PVP:SCO 2/P3HT-IDE device, respectively). The hysteresis loop enables a direct comparison of conductance between the LS and HS states at the same temperature, eliminating ordinary thermal activation effects. Here we used the current value at the hysteresis midpoint temperatures (78 °C for the SCO 1 device and 90 °C for the SCO 2 device) to obtain the conductance switching ratio,[18,23] which can be calculated as $(I_{HS} - I_{LS})/I_{LS} \times 100\%$. As shown in Fig. 1i, the PVP:SCO/P3HT-IDE devices exhibit switching ratios of approximately 50% for SCO 1 and 70% for SCO 2, which are in line with the state-of-the-art values reported in the literature.[15,18–22] The current switching behavior aligns with the SCO properties, as evidenced by the temperature-dependent magnetic and reflectivity measurements. The observed conductivity modulation within the OSC layer is attributed to the spin state switching in the SCO composite, which induces changes in the mechanical properties of the system (*vide infra*).

While pristine P3HT is one of the most extensively studied organic semiconductor (OSC) materials, its intrinsic charge transport properties remain inferior to those of inorganic conductors. Doping has been widely used as an effective strategy to significantly enhance its conductivity.[27,33] Among the various doping techniques, acid doping has recently emerged as a particularly promising approach, offering substantial improvements in not only device performance, but also environmental stability.[34] In the present study, we employed ethanesulfonic acid (ESA) as a doping agent due to its favorable properties, including excellent thermal stability, environmental compatibility, moderate acidity and low volatility.[35] The doping mechanism involves the interaction between the lone pair electrons of sulfur atoms in P3HT and the sulfonic acid groups of ESA, as illustrated schematically in Fig. 2a. ESA was introduced into a P3HT/chlorobenzene solution at two concentrations (1% and 10% by weight). The solutions were vigorously stirred at room temperature and then at 60 °C for 24 hours to ensure complete doping. As shown in Fig. S3a in the SI, the solution color deepened with increasing ESA concentration, indicating successful doping. This was further corroborated by UV-Vis absorption spectra of the spin-coated thin films (Fig. S3b). Notably, ESA itself remains transparent in the liquid state, confirming that the color change arises from the doping reaction. Electrical characterization of the doped films revealed significant enhancements in conductivity. Room-temperature current–voltage (*I–V*) measurements demonstrated that 1% and 10% ESA doping increased its conductivity by approximately two and three orders of magnitude, respectively, compared to pristine P3HT (Fig. 2b). However, higher ESA concentrations (10%) led to the formation of insoluble species after doping, resulting in less homogeneous films with visibly rougher surface topography—consistent with previous reports on other acid-doped P3HT systems.[34] Consequently, a 1% ESA concentration was selected for subsequent studies, as it provided an optimal balance between electrical conductivity and film morphology.

Importantly, we fabricated a control device (Fig. 2c) in which the top layer consists of pristine PVP (without SCO nanoparticles) on ESA-doped P3HT. This device exhibited only a quasi-linear increase in conductance with temperature without hysteresis (Fig. 2d). Next, the SCO 1 composite was incorporated into a bilayer device configuration (PVP:SCO/acid-doped P3HT) to demonstrate a proof-of-concept for current switching using the acid-doped OSC as the conducting layer. It is worth noting that SCO 1 was selected due to its lower SCO temperature. Temperature-dependent conductance measurements were carried out under varying voltage biases (ranging from 0.01 V

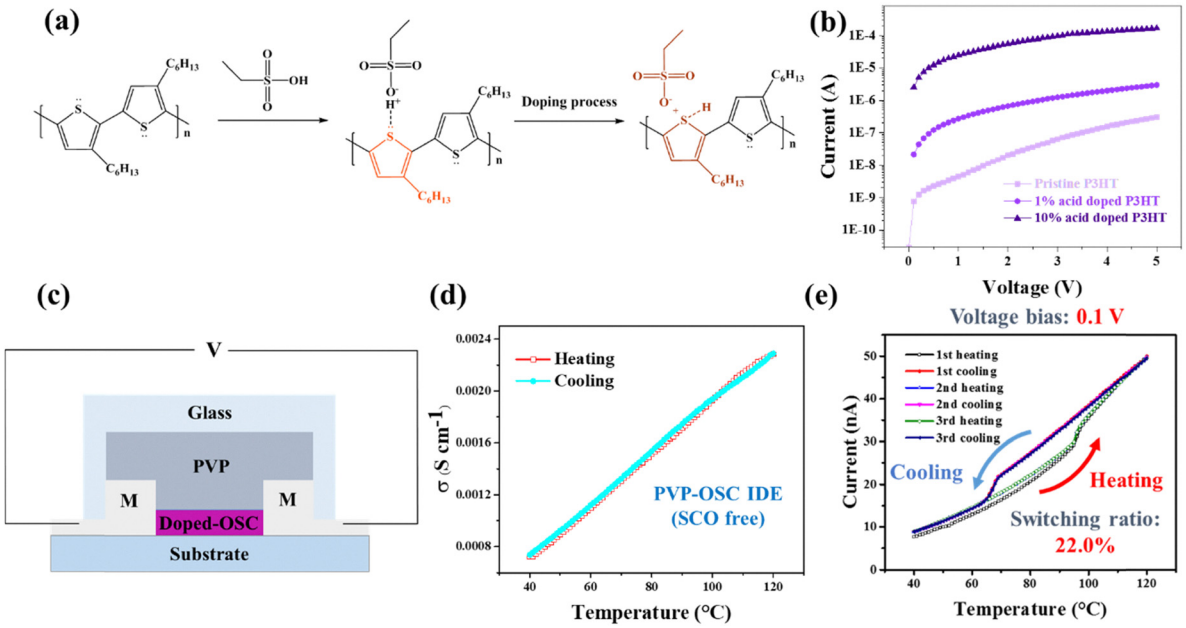

Fig. 2 (a) Schematic illustration of the doping reaction of P3HT with ESA in chlorobenzene. (b) *I*–*V* characterization of ESA:P3HT films with different doping levels. (c) A schematic cross-section of a PVP/doped-OSC IDE control device. M represents metal electrodes. (d) Temperature-dependent conductance characterization of a SCO-free control device (bilayer of 1% ESA-doped P3HT and PVP). (e) Temperature-dependent conductance characterization of a PVP:SCO 1/1% ESA-doped P3HT IDE device. Temperature-dependent current characterization of a SCO-based device at 0.1 V (dT/dt = ±5 °C min^{-1}).

to 5 V; see Fig. S4 in the SI for the complete dataset). Representative results under 0.1 V are shown in Fig. 2e. A pronounced increase in current intensity was observed near 95 °C during heating, followed by a corresponding decrease near 66 °C during cooling. Compared to the result of the SCO-free control device (Fig. 2d), the abrupt conductance change and the presence of hysteresis can be clearly attributed to the introduction of the SCO component. Within the thermal hysteresis region, the SCO complex can exist in either the low-spin (LS) or high-spin (HS) state, depending on the thermal history of the sample. The conductance switching ratio, calculated as $(I_{HS} - I_{LS})/I_{LS} \times 100\%$ at the midpoint temperature within the hysteresis loop (78 °C), was in the range of 25 ± 3%. This value is lower than that observed in PVP:SCO/pristine P3HT IDE devices (50–70%) and the difference is likely attributable to a reduction in the piezo-resistive effect of P3HT upon acid doping. A preliminary study examining the effects of device geometry, piezo-resistive layer properties, and SCO composite characteristics on current switching behavior is presented in the SI (Fig. S5 and S6), highlighting the versatility of the system.

To evaluate the piezo-resistive properties of the 1% ESA-doped P3HT film, current–voltage (*I*–*V*) measurements were conducted under externally applied hydrostatic pressure. A custom-designed printed circuit board (PCB) was used, with interdigitated electrodes connected *via* wire bonding (Fig. 3a). The PCB was placed inside a pressure cell, and the pressure was incrementally increased from 0 to 160 MPa, followed by stepwise depressurization. The conductance changes closely followed the applied pressure, as shown in Fig. 3b. The data in Fig. 3c reveal a quasi-linear increase in conductance with increasing pressure, which was reversible upon pressure release. The current switching ratio across the entire ascending pressure range was approximately 97 ± 3%. This piezo-resistive behavior can be correlated with the spin state switching observed in SCO/OSC IDE devices. During the SCO event, these devices exhibited a 25% resistance change, equivalent to the effect of an applied hydrostatic pressure of approximately 40 MPa.

Given that the OSC film is constrained between rigid metallic electrodes, preventing expansion/contraction along the current flow direction ($\varepsilon_x = 0$), the stress in this direction (σ_x) can be estimated using the following equation:

$$\varepsilon_x = \frac{\sigma_x}{E} - \nu\frac{\sigma_y}{E} = 0$$

where E and ν are Young's modulus and Poisson's ratio of the OSC film, respectively, and σ_y is the stress applied normal to the substrate plane. Using typical values for Poisson's ratio (ν = 0.2–0.3), the stress σ_x was estimated to be on the order of 10 MPa, corresponding to the observed 25% resistance change. This value is consistent with finite element simulations reported in prior work,[23] which predicted a stress of approximately 3 MPa generated by the SCO phenomenon within the OSC layer. The quasi-linear, reversible conductance increase under hydrostatic pressure confirms the inherent piezo-resistive sensitivity of the ESA-doped P3HT layer, independent of SCO switching. In contrast, the thermally induced conductance hysteresis observed in the PVP:SCO/OSC bilayers directly follows the SCO, supporting a mechanically coupled, bistable switching mechanism distinct from simple extrinsic pressure effects. These experimental results provide strong evidence for

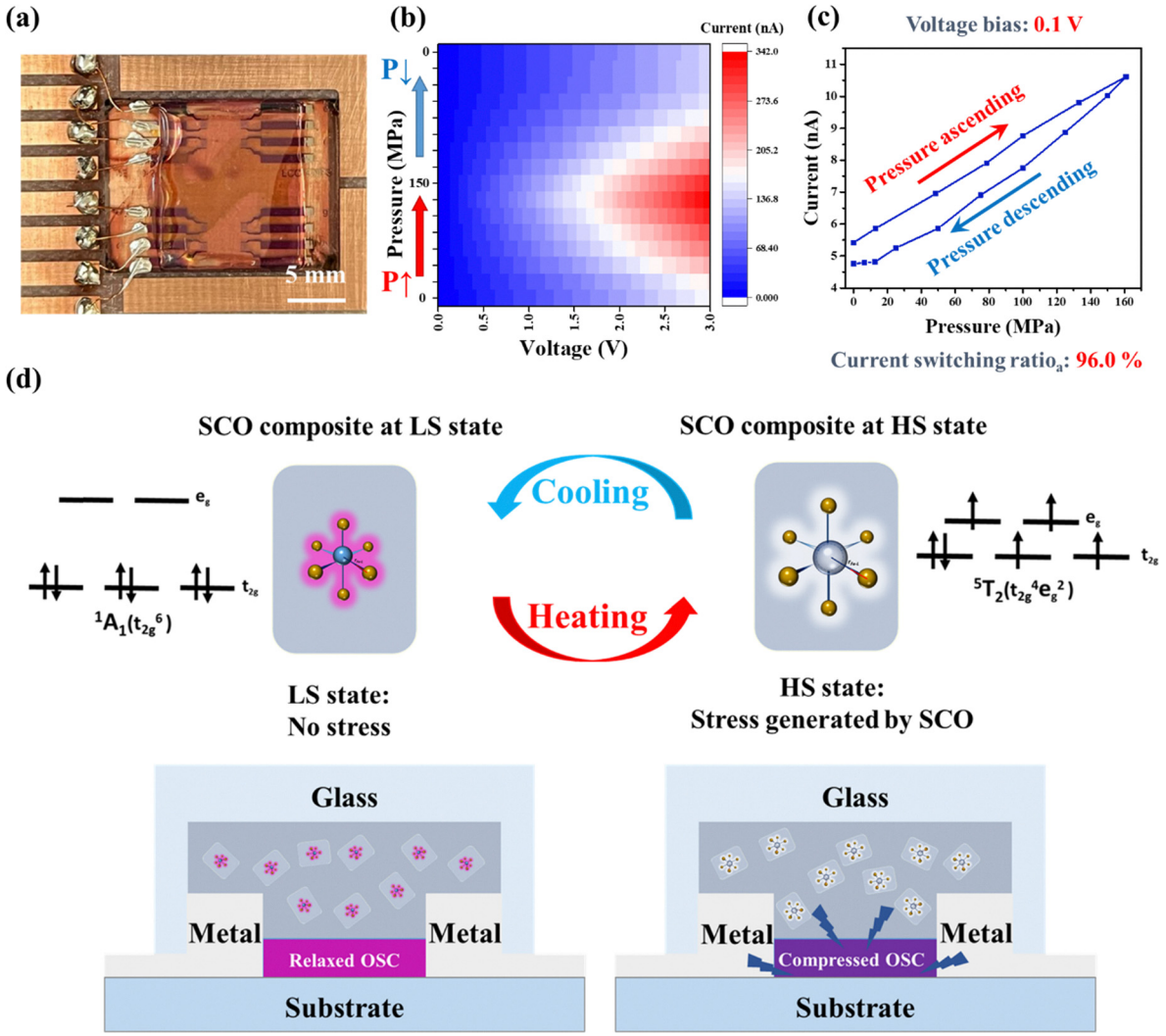

Fig. 3 (a) Photograph of the IDE device mounted on the PCB for the pressure-dependent current characterization. (b) Heat map of pressure-dependent current characteristics on a 1% ESA-doped P3HT IDE device. (c) Representative *I*–*P* curves recorded at 0.1 V applied bias for increasing and decreasing pressure values. The current switching ratio refers to the current variation when going from 0.1 to 160 MPa. (d) Schematic diagram illustrating the mechanism of how SCO modulates the conductance within the OSC layer. The volume of the SCO particles increases significantly when switching from the low-spin (LS) to the high-spin (HS) state, inducing compressive stress in the OSC layer. This transition is also accompanied by a visible color change—from purple in the LS state to white in the HS state—for both SCO1 and SCO2 samples.

the proposed strain-coupling mechanism, demonstrating its viability for sensing spin state changes in SCO/OSC bilayers. The mechanism underlying current modulation in the bilayer device structure is schematically illustrated in Fig. 3d. Upon heating, the spin-crossover (SCO) material changes from the LS to the HS state. This spin transition is accompanied by a significant volume expansion of *ca.* 10.5% of the particles due to the electronic configuration change, *i.e.* population of the antibonding e_g orbitals in the HS state.[36] This dilation of the particles gives rise to a *ca.* 2.5% expansion of the PVP:SCO composite film normal to its surface, which was observed using confocal microscopy (see Fig. S7 in the SI for more details). This value is comparable to those obtained for similar SCO–polymer composite films by means of conventional mechanical testing.[37] On the other hand, the composite film is not free to expand in the substrate plane, thus generating mechanical stress inside. When integrated on the top of an organic semiconductor (OSC) layer, this stress is transmitted, leading to the compression of the underlying OSC film. As the OSC material exhibits piezo-resistive behavior, the applied stress alters its charge transport characteristics, resulting in a reversible modulation of conductance that follows the SCO switching. This stress-coupled mechanism enables a bistable, non-volatile control of electrical properties.

To assess the cycling endurance of the device, over 100 thermally induced resistance switching cycles were performed over three days. The device was subjected to temperature ramps between 40 °C and 120 °C at a rate of ±5 °C min^{-1}, under a constant bias voltage of 0.1 V. As shown in Fig. 4a, the device retained its current switching capability throughout the cycling

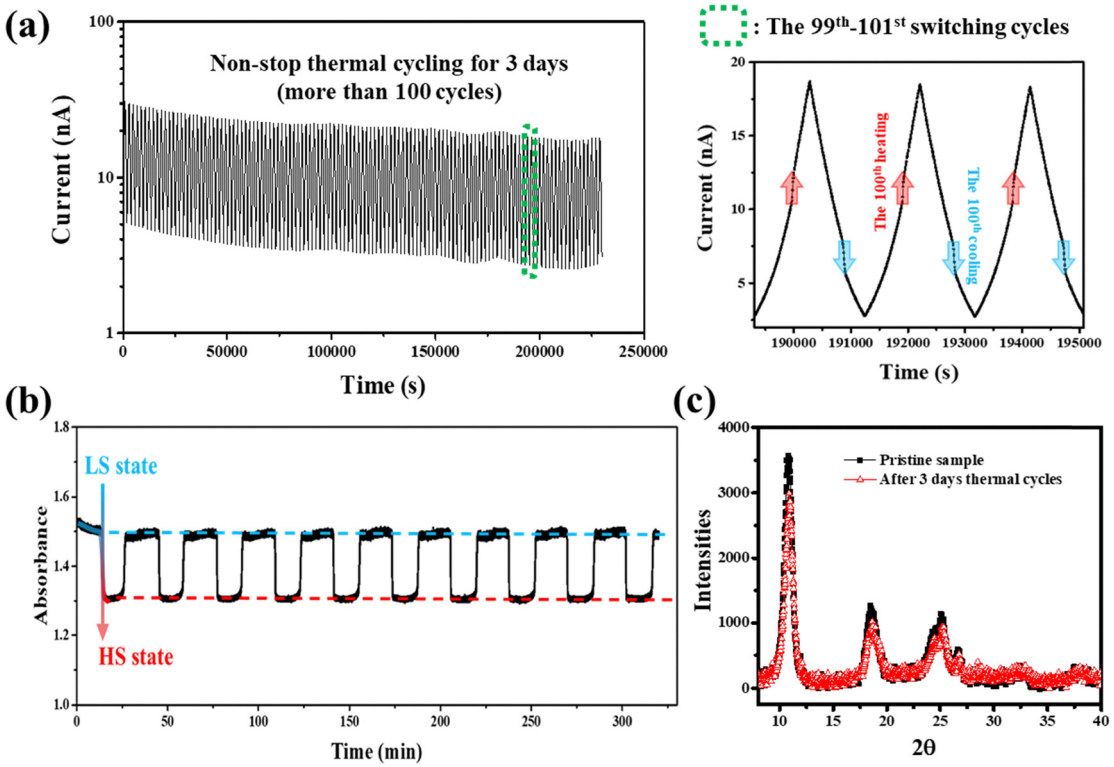

Fig. 4 (a) Current switching cycles between 40 and 120 °C in a PVP:SCO 1/1% acid-doped P3HT interdigitated electrode device under a constant bias voltage of 3 V with a temperature ramping rate of 5 °C min^{-1}. Zoomed-in views are also shown for the 99th–101st switching cycles. (b) Kinetics of changes of the optical absorbance at 350 nm, cycling between 40 and 120 °C with a temperature ramping rate of 5 °C min^{-1}. (c) XRD patterns of the PVP:SCO 1 composite film before and after thermal cycles between 40 and 120 °C for three days.

with limited fatigue. To further investigate the stability of the SCO composite, kinetics–absorbance measurements were conducted during thermal cycling (Fig. 4b). Abrupt and reversible changes in absorbance were observed, corresponding to the SCO transition. Over 300 minutes, 20 switching events were recorded without significant fatigue, and the absorbance values at the LS and HS states remained stable before and after the kinetic measurements. This indicates that the thermal cycles did not affect the intrinsic SCO properties of the composite layer. X-ray diffraction (XRD) analysis was performed before and after thermal cycling to evaluate structural stability (Fig. 4c). The XRD spectra revealed no appreciable changes in the crystal structure, further confirming the robustness of the SCO composite under repeated thermal cycling.

Conclusions

In summary, we demonstrate a robust stress-coupling mechanism in spin-crossover (SCO)–organic semiconductor (OSC) bilayer heterostructures, where spin-state switching in SCO composites directly modulates the conductance of both pristine and acid-doped P3HT *via* mechanical strain. Silica-coated SCO nanoparticles (SCO 1 and 2) with tunable transition properties (*e.g.*, hysteresis widths of 19–27 °C) were integrated into a bilayer architecture, enabling a proof-of-concept adaptive memory platform.

By employing 1% ethanesulfonic acid (ESA)-doped P3HT, we enhanced conductivity by two orders of magnitude, creating an energy-efficient strain-sensing layer. In this optimized system, reversible current modulation (25 ± 3%) synchronized with the SCO was achieved, while hydrostatic pressure experiments validated the strain-coupling mechanism—revealing a 97 ± 3% conductance change in 1% ESA-doped P3HT under 160 MPa applied pressure. The quasi-linear pressure-dependent conductance change allows for the estimation of the in-plane compressive stress (*ca.* 10 MPa) in the OSC layer due to the SCO phenomenon. This experimental result is in line with the previously reported finite element analysis data. The devices exhibited high endurance (>100 cycles) and stability.

This work establishes SCO-driven strain engineering as a versatile strategy for organic electronics, eliminating the need for external fields or complex doping. By decoupling spin-state switching from charge transport, our approach opens avenues for stress-coupled spin-organic electronics. These findings motivate future efforts to optimize room-temperature SCO materials and enhance the piezo-resistive response of organic semiconductors.

Experimental

Sample preparation

IDEs were prepared on top of glass substrates by Ti/Pt (10 nm and 200 nm, respectively) lift-off using a 5 μm negative NLOF

2035 resist (purchased from MicroChemicals). The obtained devices were rinsed successively by acetone (VLSI, 99.5%) and ethanol (VLSI, 99.9%) for 5 min under sonication. They were then dried by a nitrogen gas flow and cleaned by UV/O_3 treatment (10 min). The rest of the procedure was carried out in a glove box (O_2/H_2O < 3 ppm). Ethanesulfonic acid (>96%) and P3HT (regioregular, average Mn = 54 000–75 000 g mol^{-1}; >98% head-to-tail) were purchased from Sigma-Aldrich. For OSC deposition in the bilayer devices, a thickness of *ca.* 100 nm was obtained by spin-coating (15 mg ml^{-1} P3HT in chlorobenzene, 1200 rpm for 30 s). For the SCO deposition, the SCO nanoparticles (synthesized as described in ref. 30) and PVP (40–50G, purchased from Sigma-Aldrich) were mixed with ethanol at concentrations of 50 mg ml^{-1} and spin-coated on top of the OSC layer at 1200 rpm for 30 s (thickness of *ca.* 450 nm), followed by thermal annealing (80 °C, 10 min). Finally, for the device encapsulation, a glass slide was placed on the sample and sealed all around with a UV-curable epoxy (DELO Katiobond LP655). The doping process was described in the main text. Since the color of highly doped P3HT is rather deep to facilitate optical absorption studies (Fig. S3b), a thin film (*ca.* 15 nm) of doped (0, 1% and 10%) P3HT was prepared (10 mg ml^{-1} P3HT in chlorobenzene, 3000 rpm for 30 s). These films were used to compare the optical absorption and electrical conductance.

Sample characterization

Temperature-dependent magnetic susceptibility measurements were performed using a Quantum Design MPMS-XL magnetometer at heating and cooling rates of 2 K min^{-1} in a magnetic field of 10 kOe. The SCO phenomenon in the composite films was detected by measuring the temperature-dependent optical absorption spectrum using a Cary 50 (Agilent) spectrophotometer and a THMS600 (Linkam Scientific) heating–cooling stage. Atomic force microscopy (AFM) surface topography images were acquired under ambient conditions in tapping mode using a SMART-SPM (Horiba) equipped with HQ:NSC15/Al BS probes (MikroMasch, 40 N m^{-1}, 300 kHz). Variable temperature confocal microscopy measurements were conducted using an S-NEOX (Sensofar) instrument with a *z*-resolution of *ca.* 4 nm, in combination with the THMS600 stage. Current–voltage and current-temperature characteristics of the IDE junctions were analyzed using a Keithley-6430 source-meter and a heating–cooling probe station (Linkam Scientific HFS350EV-PB4) equipped with gold-tipped tungsten probes. For electrical characterization under an externally applied pressure, the IDEs were connected by wire-bonded flexible leads to high-pressure feedthrough connectors in a commercial high-pressure cell (Novocontrol Technologies). Silicone oil was used as a pressure-transmitting medium, and the electrode assembly was fully immersed in oil to provide hydrostatic conditions. X-ray diffraction (XRD) experiments were carried out in a PANalytical X'Pert PRO MPD system using Cu-Kα radiation with a parallel-beam configuration.

Conflicts of interest

The authors declare no conflict of interest.

Data availability

The data that support the findings of this study are available from the corresponding author, upon reasonable request.

Additional sample characterization information is provided in the SI (pdf). See DOI: **https://doi.org/10.1039/d5tc02153g**

Acknowledgements

This work was supported by the LAAS-CNRS micro and nanotechnologies platform, a member of the Renatech French national network. A. B. is grateful for the funding from the European Research Council (ERC) under the European Union's Horizon 2020 research and innovation program (Grant Agreement No. 101019522). G. M. and I. S. acknowledge the support from the Occitanie region, the European Regional Development Fund (ERDF), and the French government, through the "France 2030" and "Programme d'Investissements d'Avenir" projects managed by the National Research Agency (ANR) with the reference numbers "ANR-22-EXES-0015" and ANR-21-ESRE-0012, respectively.

References

1 B. L. Feringa and W. R. Browne, *Molecular switches*, John Wiley & Sons, 2011.
2 S. H. Yu, S. Z. Hassan, C. So, M. Kang and D. S. Chung, *Adv. Mater.*, 2023, **35**, 2203401.
3 G. Molnár, S. Rat, L. Salmon, W. Nicolazzi and A. Bousseksou, *Adv. Mater.*, 2018, **30**, 1703862.
4 R. S. Williams, S. Goswami and S. Goswami, *Nat. Mater.*, 2024, **23**, 1475–1485.
5 P. Gütlich, A. Hauser and H. Spiering, *Angew. Chem., Int. Ed. Engl.*, 1994, **33**, 2024–2054.
6 *Spin-crossover materials: properties and applications*, ed. M. A. Halcrow, John Wiley & Sons, 2013.
7 *Spin crossover in transition metal compounds I*, ed. P. Gütlich and H. A. Goodwin, Springer Science & Business Media, 2004.
8 K. S. Kumar and M. Ruben, *Coord. Chem. Rev.*, 2017, **346**, 176–205.
9 K. Ridier, A.-C. Bas, Y. Zhang, L. Routaboul, L. Salmon, G. Molnár, C. Bergaud and A. Bousseksou, *Nat. Commun.*, 2020, **11**, 3611.
10 M. Piedrahita-Bello, J. E. Angulo-Cervera, A. Enriquez-Cabrera, G. Molnár, B. Tondu, L. Salmon and A. Bousseksou, *Mater. Horiz.*, 2021, **8**, 3055–3062.
11 G. Hao, A. Mosey, X. Jiang, A. Yost, K. Sapkota, G. Wang, X. Zhang, J. Zhang, A. N'Diaye and R. Cheng, *Appl. Phys. Lett.*, 2019, 114.
12 S. P. Vallone, A. N. Tantillo, A. M. Dos Santos, J. J. Molaison, R. Kulmaczewski, A. Chapoy, P. Ahmadi, M. A. Halcrow and K. G. Sandeman, *Adv. Mater.*, 2019, **31**, 1807334.
13 K. Ridier, Y. Zhang, M. Piedrahita-Bello, C. M. Quintero, L. Salmon, G. Molnar, C. Bergaud and A. Bousseksou, *Adv. Mater.*, 2020, **32**, 2000987.

14 H. J. Shepherd, I. y A. Gural'skiy, C. M. Quintero, S. Tricard, L. Salmon, G. Molnár and A. Bousseksou, *Nat. Commun.*, 2013, **4**, 2607.
15 J. Dugay, M. Aarts, M. Giménez-Marqués, T. Kozlova, H. Zandbergen, E. Coronado and H. Van Der Zant, *Nano Lett.*, 2017, **17**, 186–193.
16 M. D. Manrique-Juarez, F. Mathieu, A. Laborde, S. Rat, V. Shalabaeva, P. Demont, O. Thomas, L. Salmon, T. Leichle and L. Nicu, *Adv. Funct. Mater.*, 2018, **28**, 1801970.
17 S. Rat, M. Piedrahita-Bello, L. Salmon, G. Molnar, P. Demont and A. Bousseksou, *Adv. Mater.*, 2018, **30**, 1705275.
18 E. P. van Geest, K. Shakouri, W. Fu, V. Robert, V. Tudor, S. Bonnet and G. F. Schneider, *Adv. Mater.*, 2020, **32**, 1903575.
19 J.-F. Dayen, N. Konstantinov, M. Palluel, N. Daro, B. Kundys, M. Soliman, G. Chastanet and B. Doudin, *Mater. Horiz.*, 2021, **8**, 2310–2315.
20 N. Konstantinov, A. Tauzin, U. N. Noumbé, D. Dragoe, B. Kundys, H. Majjad, A. Brosseau, M. Lenertz, A. Singh and S. Berciaud, *J. Mater. Chem. C*, 2021, **9**, 2712–2720.
21 C. Boix-Constant, V. Garcia-Lopez, E. Navarro-Moratalla, M. Clemente-Leon, J. L. Zafra, J. Casado, F. Guinea, S. Mañas-Valero and E. Coronado, *Adv. Mater.*, 2022, **34**, 2110027.
22 M. Gavara-Edo, R. Cordoba, F. J. Valverde-Muñoz, J. Herrero-Martin, J. A. Real and E. Coronado, *Adv. Mater.*, 2022, **34**, 2202551.
23 Y. Zhang, S. E. Alavi, I. Soroceanu, D. W. Kamau, A. Rotaru, I. Séguy, L. Salmon, G. Molnár and A. Bousseksou, *Adv. Electron. Mater.*, 2025, **11**, 2400590.
24 R. Torres-Cavanillas, M. Gavara-Edo and E. Coronado, *Adv. Mater.*, 2024, **36**, 2307718.
25 J. Villalva, A. Develioglu, N. Montenegro-Pohlhammer, R. Sánchez-de-Armas, A. Gamonal, E. Rial, M. García-Hernández, L. Ruiz-Gonzalez, J. S. Costa and C. J. Calzado, *Nat. Commun.*, 2021, **12**, 1578.
26 D. Yuan, W. Liu and X. Zhu, *Chem. Soc. Rev.*, 2023, **52**, 3842–3872.
27 Y. Xu, H. Sun, A. Liu, H. H. Zhu, W. Li, Y. F. Lin and Y. Y. Noh, *Adv. Mater.*, 2018, **30**, 1801830.
28 B. Dieny, I. L. Prejbeanu, K. Garello, P. Gambardella, P. Freitas, R. Lehndorff, W. Raberg, U. Ebels, S. O. Demokritov and J. Akerman, *Nat. Electron.*, 2020, **3**, 446–459.
29 S. T. Han, Y. Zhou and V. Roy, *Adv. Mater.*, 2013, **25**, 5425–5449.
30 Y. Zan, L. Salmon and A. Bousseksou, *Nanomaterials*, 2021, **11**, 3169.
31 K. Lünser, E. Kavak, K. Gürpinar, B. Emre, O. Atakol, E. Stern-Taulats, M. Porta, A. Planes, P. Lloveras and J.-L. Tamarit, *Nat. Commun.*, 2024, **15**, 6171.
32 Y. S. Koo and J. R. Galan-Mascaros, *Adv. Mater.*, 2014, **26**, 6785–6789.
33 A. Dash, S. Guchait, D. Scheunemann, V. Vijayakumar, N. Leclerc, M. Brinkmann and M. Kemerink, *Adv. Mater.*, 2024, **36**, 2311303.
34 E. H. Suh, J. G. Oh, J. Jung, S. H. Noh, T. S. Lee and J. Jang, *Adv. Energy Mater.*, 2020, **10**, 2002521.
35 A. Hayyan, F. S. Mjalli, M. A. Hashim, M. Hayyan, I. M. AlNashef, S. M. Al-Zahrani and M. A. Al-Saadi, *Bioresour. Technol.*, 2011, **102**, 9564–9570.
36 D. Paliwoda, L. Vendier, L. Getzner, F. Alabarse, D. Comboni, B. Martin, S. E. Alavi, M. Piedrahita Bello, L. Salmon, W. Nicolazzi, G. Molnár and A. Bousseksou, *Cryst. Growth Des.*, 2023, **23**, 1903–1914.
37 S. E. Alavi, B. Martin, Y. Zan, X. Yang, M. Piedrahita-Bello, W. Nicolazzi, J.-F. Ganghoffer, L. Salmon, G. Molnár and A. Bousseksou, *Chem. Mater.*, 2023, **35**, 3276–3289.

